Advanced Optical Materials

ADVANCED OPTICAL MATERIALS
www.advopticalmat.de

RESEARCH ARTICLE

Self-Rolled-up Te/Graphene Photothermoelectric Detector Enhanced with Built-in Field for Imaging and Convolution Processing

Mingze Ma[1,2] | Yaru Shi[3,4] | Xubing Ye[5] | Tianjun Cai[1,2] | Ziyu Zhang[1,2] | Zhiqun Zhang[1,2] | Zhiyuan Qiao[1,2] | Jiayang You[1,2] | Binmin Wu[6] | Xuansheng Pan[1,2] | Tingqi Wu[7] | Xugao Cui[1,2] | Tao Sun[8,9] | Shaojuan Li[3,4] | Yongfeng Mei[1,2] | Gaoshan Huang[1,2]

[1]International Institute for Intelligent Nanorobots and Nanosystems, State Key Laboratory of Surface Physics, State Key Laboratory of Photovoltaic Science and Technology, and College of Intelligent Robotics and Advanced Manufacturing, Fudan University, Shanghai, P. R. China | [2]Zhejiang Key Laboratory of Extreme Environment Functional Materials, Yiwu Research Institute of Fudan University, Yiwu, Zhejiang, P. R. China | [3]State Key Laboratory of Luminescence Science and Technology, Changchun Institute of Optics, Fine Mechanics and Physics, Chinese Academy of Sciences, Changchun, Jilin, P. R. China | [4]University of Chinese Academy of Sciences, Beijing, P. R. China | [5]Shenzhen International Graduate School, Tsinghua University, Shenzhen, Guangdong, P. R. China | [6]State Key Laboratory of Infrared Physics, Shanghai Institute of Technical Physics, Chinese Academy of Sciences, Shanghai, P. R. China | [7]Shanghaitech Material and Device Lab, ShanghaiTech University, Shanghai, P. R. China | [8]State Key Laboratory of High End Heavy Load Robots, Foshan, P. R. China | [9]Artificial Intelligence Research Center, Midea Group, Shanghai, P. R. China

Correspondence: Shaojuan Li (lishaojuan@ciomp.ac.cn) | Yongfeng Mei (yfm@fudan.edu.cn) | Gaoshan Huang (gshuang@fudan.edu.cn)

Received: 27 January 2026 | **Revised:** 12 March 2026 | **Accepted:** 9 April 2026

Keywords: image feature extraction | self-construct convolution kernel | tellurium-Graphene heterostructure | tubular photothermoelectric detector

ABSTRACT

Amidst the rapid evolution of the information society, there is a pressing demand for photodetectors which integrate high performance with imaging and processing capabilities. However, implementing traditional image processing relying on predefined convolution kernels inherently suffers from constrained adaptability and is difficult in individual optimization. Here, we introduce a self-rolled-up Te/Graphene photothermoelectric detector (STGP), pioneering a physics-response-driven self-construct convolution kernel strategy rooted in its wide-angle detection performance for advanced image feature extraction. The STGP leverages a tubular morphology that efficiently enhances light absorption via light-trapping effect while the built-in electric field is established at the Te/Graphene interface due to their work function difference, which promotes the directional transport of photo-thermally excited carriers, substantially suppressing interfacial recombination losses. The STGP realizes a high voltage responsivity of 259 $V W^{-1}$ at 940 nm and an ultrafast response time. Functionally, the unique tubular geometry enables exceptional wide-angle detection, which is used as the basis for self-construct convolution kernels and achieve effective image sharpening and edge extraction. This work not only provides a novel built-in field enhancement strategy for photothermoelectric detectors but also establishes a new paradigm for in-sensor computing by integrating the material's physical response with computational functions.

1 | Introduction

With the rapid development of the information society, photodetection has demonstrated increasingly critical importance across numerous fields such as imaging, communications, environmental monitoring, and life sciences [1–3]. Particularly in the optical imaging field, the emergence of high-performance detectors has not only enhanced imaging resolution and sensitivity but also enabled multifunctional imaging modalities [4]. Among various emerging detection mechanisms, photothermoelectric (PTE) photodetection has attracted significant research interest [5–7]. The conversion of incident light into localized heat within the absorption layer, generating a temperature gradient through thermal diffusion, which subsequently induces a thermoelectric voltage output. Owing to this distinctive operational principle, PTE detectors exhibit intrinsic broadband spectral sensitivity, maintaining high responsivity from visible to near-infrared and even longer wavelengths. The utilization of self-rolled-up nanomembrane technology forms a unique tubular geometry, which enhances light-matter interaction through a light-trapping effect, significantly promoting light absorption efficiency toward high responsivity [8–10]. However, the intrinsic operational mechanism of PTE detectors, which relies on thermally excited carriers and the relatively slow establishment of a temperature gradient, often results in a limited response speed. This speed constraint encounters a significant challenge, particularly for advanced optical imaging and real-time computation applications where both high spatial resolution and fast acquisition rates are non-negotiable requirements [8]. Previously in literature, due to the differences in work function and band alignment between dissimilar materials, a built-in electric field is naturally constructed at the interface, and the direction of this field correlates with the charge carrier transport path [6]. When the localized temperature gradient is established, thermally excited carriers experience not only diffusion but also drift driven by the built-in electric field, enabling more efficient separation and directional transport [11]. Compared to relying solely on thermally driven carrier diffusion, the synergy between the built-in field and the PTE effect accelerates the directional transport of thermally excited carriers while significantly mitigating recombination losses [12]. This mechanism fundamentally ensures the simultaneous achievement of high responsivity and rapid response speed, laying a physical foundation for high quality imaging process that demands both a superior signal-to-noise ratio and fast data acquisition.

In addition, with the widespread application of photodetection technologies, the real-time image processing capabilities of traditional processors have struggled to meet growing demands [13, 14]. The traditional convention processing, relying on predefined convolution kernels, is typically confined to basic feature extraction and fundamentally encounters difficulties in achieving a structurally optimized processing configuration for best overall performance. This gap has driven the development of photodetectors toward integrating image processing functions, such as convolution processing, directly within the detectors. However, most existing convolution processing solutions still rely on mathematically predefined convolution kernels or external gate voltage control which is seldom related to the detector's intrinsic characteristics [15–18]. The additional energy consumption and circuit complexity introduced by external gate control also limit the application in high-speed and low-power systems. Furthermore, the self-construct kernels suffer from a disconnection between mathematical kernels and the device's photoresponse, resulting in poor adaptability, insufficient robustness, and difficulties in achieving high-fidelity and high-resolution feature extraction [17]. Therefore, the key direction for advancing image processing is to construct convolution kernels closely linked to the device's output with inherent physical response properties in order to achieve better detail enhancement and feature extraction [19–22].

In this work, we fabricated the self-rolled-up Te/Graphene heterostructure PTE detector (STGP), where Te was selected as for its exceptional Seebeck coefficient and broad spectral absorption, coupling with high-mobility Graphene to establish built-in electric field that accelerates hot-carrier separation and transport. The proposed STGP utilizes the built-in field for high-performance and adaptive image convolution processing according to the wide-angle photodetection. By pioneering the design of a tubular geometry and leveraging the modulation of its built-in electric field, we have achieved both ultrahigh responsivity and ultrafast response speed. The present work demonstrates that the device achieves the highest responsivity of 259 V W^{-1} with a response time as low as 192 µs at 940 nm, providing stable and efficient output for imaging. Optically, STGP device exhibits unique advantages in wide-angle detection and polarization-sensitive response. The tubular structure enables efficient reception of incident light from various angles, maintaining stable response across a 140° range which significantly outperforms conventional planar detectors. Moreover, the geometric advantages of the tubular configuration allow STGP to response sensitively to light with different polarization angles, demonstrating its potential for polarized light detection and polarization imaging. Beyond designed optimization, according to the wide-angle detection capability of the STGP detector, we directly translated photocurrent response characteristics at different incident angles into elements of convolution kernels, constructing a fully experimental data-driven convolution kernels. This approach ensures that the convolution kernels originate from the actual physical response of the device, providing inherent physical consistency and adaptability. Furthermore, wide-angle detection offers multi-dimensional photovoltage, enabling the convolution kernels to exhibit stronger differentiation and directionality in the spatial domain, thereby flexibly adapting to diverse image feature processing requirements by iterating through convolution kernels derived from wide-angle photovoltage values. Using this method, we successfully enhanced contrast and detail visibility for image sharpening while highlighting geometric contours and edge features for edge extraction. This approach breaks through the limitations of traditional predefined kernels, demonstrating a novel physics-driven strategy for image processing and providing strong support for the development of high-performance image processing system.

2 | Results and Discussion

2.1 | Fabrication and Architecture of the Photodetector

Figure 1a schematically illustrates the structure of the STGP. The STGP we designed includes self-rolled-up structure consisting of a Te layer, a monolayer Graphene, SiN_x pre-stressed bilayer, and Al_2O_3 protection layer, Ti/Au electrodes (part of which are rolled into the tube), Ge sacrificial layer, and a thermally oxidized silicon wafer as a substrate. The STGP was prepared by selectively etching away the Ge sacrificial layer while the release of the pre-stressed SiN_x bilayer led to the rolling of the multi-layered nanomembrane, the ALD-deposited Al_2O_3 layer

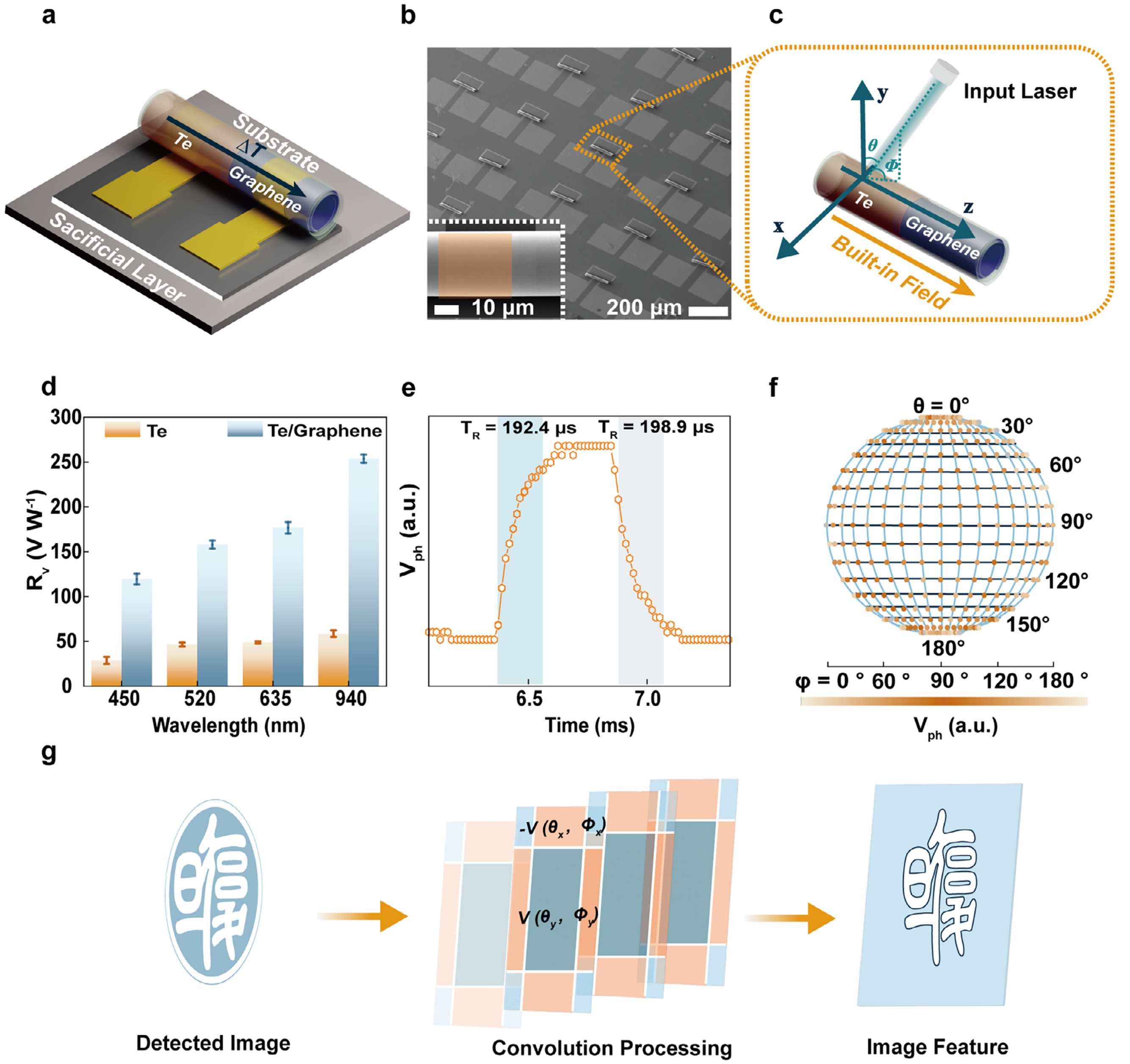

FIGURE 1 | Structure and performance of STGP for imaging and convolution processing. (a) Schematic of the heterostructure of STGP. (b) A 4 × 4 array of STGPs. (c) Schematic of the photodetection and the direction of built-in field. (d) Comparation of the photovoltage responses of Te photodetector and STGP. (e) Photoresponse time of the STGP irradiated by 940 nm laser. (f) 3D angular mapping of the photovoltage V_{ph} in spherical coordinates. (g) Schematic diagram of the image convolution processing to feature extraction by using the convolution kernels.

was integrated to safeguard Graphene from damage during the etching while guiding the directional self-rolling. The details of the preparation process of the structure of the device are specified in Figures S1 and S2, and side-view SEM (scanning electron microscopy) images of a typical STGP with a radius of ∼19 μm are demonstrated in Figure S3. In Figure 1b, we demonstrate the fabrication of 4 × 4 array of STGPs, and the inset illustrates the magnified view of a tubular structure, where the Te part (pseudo-colored orange) can clearly be observed while the extreme thinness and weak atomic number contrast of monolayer Graphene leads its signal to be drowned out in SEM imaging. We conduct the thermal simulation of the device when it is illuminated by a laser (Figure 1c) to investigate the details of thermal diffusion in the current PTE device. The simulation result in Figure S4 demonstrates the formation of a temperature gradient when Te layer is irradiated, with Te layer acting as the hot part while Graphene as the cold part. The direction of thermal diffusion along z direction in Figure 1c and the temperature gradient provide an efficient way to produce the thermoelectric voltage. Moreover, due to the thermal energy localization and the light trap effect inside the tube wall provided by tubular structure [8, 23–26], the STGP achieved almost 582 higher photovoltage response comparing to the planar Te/Graphene heterostructure PTE photodetector (PTGP) under 450 nm laser (Figure S5). We also analyzed the response performance of both the tubular Te layer PTE detector and STGP. As evidenced by Figure 1d, under same identical wavelength and incident laser power density, the STGP exhibits a significantly higher responsivity. This result indicates that the performance enhancement should be connected with the Te/Graphene heterostructure, and the built-in field directed from Te layer to Graphene (Figure 1c; Figure S6) plays important role. In our work, the response time of the detector was further investigated. The rise time (T_R) and decay time (T_D) are defined as the time required for output electrical signal to increase from 10% to 90% and to decrease from 10% to 90% of its final steady-state values respectively. For our STGP, $T_{R,}$ and T_D are respectively determined to be 192.4 and 198.9 μs under 940 nm laser, as shown in Figure 1e. The fast response speed that STGP demonstrates further confirms the role of the built-in field takes in facilitating carrier separation (Figure S6), and the detailed mechanism will be discussed later [8]. The higher response speed provides the more accurate imaging platform comparing to the tubular Te layer photodetector. It is worth noting that the CMOS-compatible characteristics during the fabrication pave an accessible way for the mass production of the devices. Experimentally, we selected twenty-five devices from the array, and the results in Figure S7 demonstrate that different devices exhibit the uniformity of detection performance under illumination at the same power density (450 nm laser with power of 169 μw and spot size of ~780 μm^2), suggesting stability of self-rolled-up tubular structure and the potential of current STGP in practical applications.

In addition, the geometric feature of the tubular structure endows the device with wide-angle detection performance, overcoming the limitation of inherent incident angle constraints comparing with the planar detectors, and this feature is crucial for image convolution processing. For this application, the detected image acquired from the STGP is subjected to convolution processing using convolution kernels attributed to the photo response by incident light (450 nm laser with power of 169 μw and spot size of ~20 cm^2) from a broad angle range (Figure S8). As shown in Figure 1f, 3D angular mapping shows the photovoltage response in spherical coordinates, and the longitudes and latitudes define the angles θ and ϕ respectively. The good photovoltage responses at different angles in spherical coordinates further reveals the wide-angle detection ability of the STGP, and the photovoltage values provide a sufficient data foundation for image processing via self-constructed convolution kernels. Convolution processing provides a powerful approach to extract image features from these original images, as it enables selective enhancement of specific characteristics, such as sharpness and edge extraction, by applying self-designed convolution kernel [14, 16]. Here, Figure 1g schematically depicts the convolutional process from original image to the image feature. In this process, we mapped the photovoltage values obtained from wide-angle photodetection into the self-construct convolution kernel, and image features are accordingly obtained by using different convolution kernels.

2.2 | Microstructural Characterizations of STGP

STGP is the integrated device consisting of different materials, and pre-stressed SiN_x bilayer is crucial in the rolling process. A theoretical model was set up to disclose the rolling behavior and the material properties set in theoretical model are listed in Table S1. In this simplified model, the nanomembrane consists of only important layers: bottom SiN_x layer, upper SiN_x layer, and top Te layer. The bottom SiN_x layer is under the compressive stress before releasing while the upper SiN_x layer is under the tensile stress. After the releasing and rolling up of the nanomembrane, elastic energy should decrease to the minimal in order to realize a stable state [27–29]. According to the literature, the diameter of the self-rolled-up tubular structure can be calculated by following equations [28]:

$$R = \frac{2\sum_{i=1}^{n} E_i' t_i \left[y_i^2 + y_i y_{i-1} + y_{i-1}^2 - 3y_b\left(y_i + y_{i-1} - y_b\right)\right]}{3\sum_{i=1}^{n} E_i' t_i \left(y_i + y_{i-1} - 2y_b\right)\left(c - \eta_i \varepsilon_i^0\right)} \quad (1)$$

$$y_b = \frac{\sum_{i=1}^{n} E_i' t_i \left(y_i + y_{i-1}\right)}{2\sum_{i=1}^{n} E_i' t_i} \quad (2)$$

$$c = \frac{\Sigma_{i=1}^{n} E_i' t_i \eta_i \varepsilon_i^0}{\sum_{i=1}^{n} E_i' t_i} \quad (3)$$

$$y_i = \sum\nolimits_{i=1}^{n} t_i \quad (4)$$

where E_i' is the effective Young's Modulus of each layer and i = 1, 2, 3 respectively represent bottom SiN_x, upper SiN_x, and Te layers, t_i means the respective thickness of each layer, and ε_i^0 means the initial strain. In our experiment, we deposited Te layer with different thicknesses on SiN_x bilayer to tune the diameter of the STGP (Figure S9). The theoretical results and experiment results are in good consistency when ε_3^0 was taken as −0.84% (Figure 2a). This means the top Te layer is under compressive strain before the releasing and rolling. More, the Te layer play a crucial part in absorbing light and achieving PTE conversion, and thus the crystal structure of Te layer was investigated. Experimentally, Te layer was deposited by magnetic sputtering, and then annealed from 210°C to 280°C. In corresponding X-ray diffraction (XRD) patterns (Figure 2b), we observed that the (100), (101), and (110) diffraction peaks achieved their maximum intensities and minimum full widths at half maximum after being annealed at 260°C. This indicates that the Te layer attained its optimal crystal quality at this temperature, which not only ensures superior crystallinity but also avoids potential Te degradation due to evaporation and excessive thermal stress [30]. Given that the performance of PTE detectors strongly depends on the crystallinity of the material, the 260°C annealing was selected in producing STGP. The microstructural properties of the structure were further characterized by Raman spectroscopy. In Figure 2c, the polarized Raman spectroscopy of Te proves that the symmetric stretching A_1 mode (~121cm^{-1}) and in-plane bending E_2 mode (~141 cm^{-1}) show intensity evolution under laser with rotating polarization. The most significant implication of this evolution lies in the geometric feature connected with the self-rolled-up tubular structure, which provides optical anisotropy [8, 9]. In addition, according to the Raman line scan along the direction perpendicular to the rolling direction (Figure 2d) and single-point Raman test at heterostructure region (Figure S10), the deposition of Te layer and the transfer of monolayer Graphene at predetermined locations are confirmed [31, 32]. As illustrated in Figure S11, Raman line scanning is tested along the direction

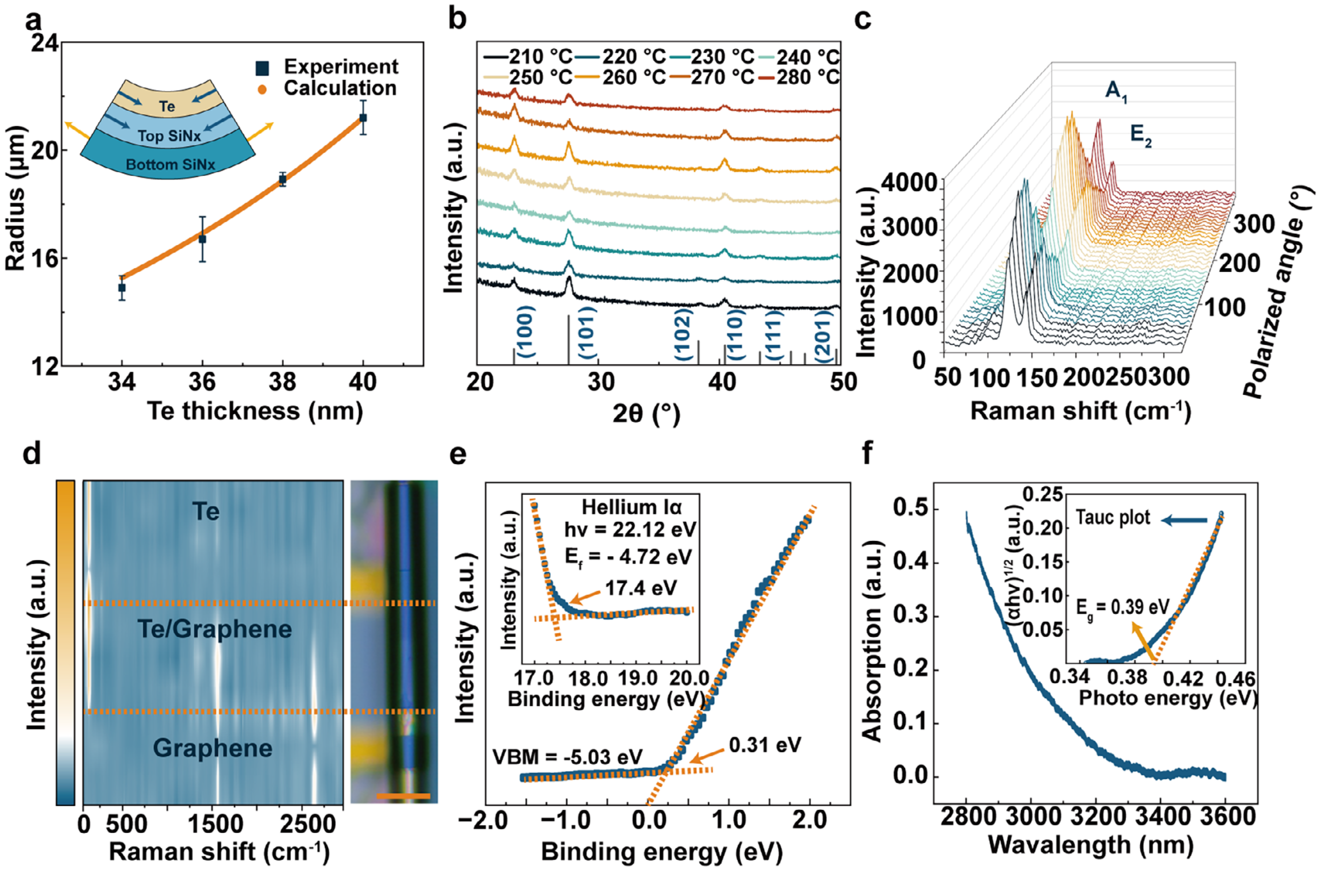

FIGURE 2 | Microstructural characterizations of STGP. (a) Theoretical calculation and experiment measurement of the diameter as functions of the thickness of top Te layer. (b) XRD patterns of Te layer at different annealing temperatures. (c) Angle-resolved polarized Raman spectra of Te layer, with A_1 and E_2 peaks marked. (d) Raman mapping along the direction parallel to the axis of the tubular structure. The optical microscopy image of the measured tubular structure is shown in the right panel. Scale bar, 40 μm. (e) UPS spectrum of the valence-band region of Te layer to calculate VBM. Inset: secondary electron cutoff spectrum of Te layer to calculate the Fermi level. f) FTIR spectrum of Te layer. Inset is the corresponding Tauc plot.

perpendicular to the axis of the tubular structure, aiming to observe the shifts of the Graphene G and 2D peaks influenced by the stress during the rolling-up process. Specifically, the G peak is observed in the range of 1581–1585 cm^{-1}, demonstrating blueshift compared to the theoretical value of 1580 cm^{-1} while the 2D peak in the range of 2682–2690 cm^{-1} show blueshift to theoretical value of 2682 cm^{-1}. The observed shifts of the Raman peaks thus suggest a compressive strain in the Graphene [32].

Figure 2e presents the ultraviolet photoelectron spectroscopy (UPS) results of the Te layer, which are employed to determine the positions of Fermi level (E_f) and valence band maximum (VBM). Using the He Iα excitation source (hν = 21.22 eV), the secondary electron cutoff energy is measured to be $E_{\mathrm{cutoff}} = 17.4$ eV, while E_f is around −4.72 eV. The VBM lies 0.31 eV below the Fermi level, and thus the position is determined to be −5.03 eV. According to the absorption spectrum measured by Fourier transform infrared spectrometer (FTIR, in Figure 2f) and corresponding Tauc plot plotted in the inset, we concluded that the optical bandgap of Te is around 0.39 eV. When Te and Graphene contact to form a heterostructure, the built-in electric field at the interface was established and facilitated the directional transport of thermally excited carriers and suppresses recombination, enhancing the performance of STGP.

2.3 | Carrier Transportation Properties in the Device

Among the STGP devices, in order to explain the positive role of the built-in field for photodetection, we conducted the charge-density difference simulation by Bader-charge analysis with the assistance of Visualization for Electronic and Structure Analysis [33]. As shown in Figure 3a, Te layer acts as the electron donator while Graphene acts as the acceptor which leads to a built-in filed from Te to Graphene. It could be observed in Figure 3b that the energy band of Graphene maintains its Dirac cone structure and the electronic states of C atoms are concentrated near the Dirac point (see the dashed line in Figure 3b), which provides the firm foundation of high-speed carrier transport in photodetection [9, 34]. Aiming to further study the band relationship between Te layer and Graphene, we conducted Kelvin probe force microscopy (KPFM) on the heterostructure. Figure 3c illustrated the surface potential of Te/Graphene and Graphene. The results exhibit the maximum surface potential of Te/Graphene heterostructure is about 80 meV higher than that of Graphene, suggesting that Fermi level alignment is achieved by Te pulling up the Fermi level of Graphene upon contact, as is schematically shown in the energy band profile in Figure 3d. The corresponding electrons transfer from Te to Graphene thus constructs the

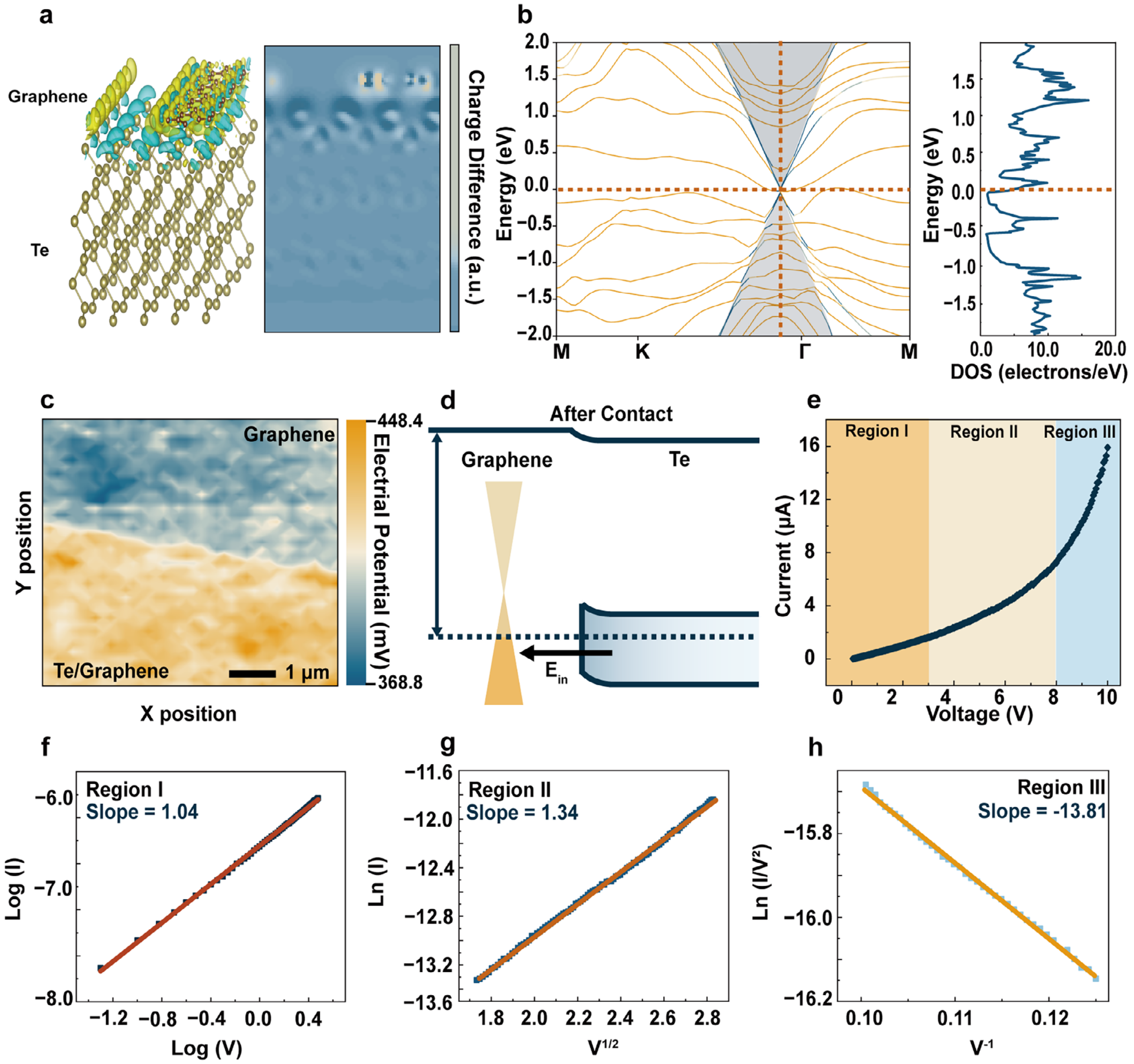

FIGURE 3 | Charge transport behavior of STGP and the underneath mechanism. (a) Schematic of the simulated structure (left) of Te/Graphene heterostructure with its isosurfaces of charge difference density and the distribution of charge-density difference of the heterostructure (right). The yellow and blue regions identify Graphene as the electron acceptor and Te as the electron donor, respectively. (b) Simulated energy band of Te and Graphene and the density of states (DOS) of electrons contributed by carbon. (c) KPFM image from Te/Graphene heterostructure to monolayer Graphene. (d) Band structure of Te/Graphene heterostructure and the built-in field at the interface is labeled. (e) *I–V* curve of STGP in a linear coordinate. According to the different carrier transport mechanisms, the *I–V* curve can be divided into three regions: (f) Region I (0–3 V) dominated by Ohmic transportation, (g) Region II (3–8 V) dominated by Schottky emission, and (h) Region III (8–10 V) dominated by Fowler-Nordheim (FN) tunneling.

built-in field directed from Te to Graphene [35]. During detection, the photo-thermally excited electron-hole pairs are subject to directional separation driven by the built-in electric field, which significantly suppresses interfacial recombination losses (Figure S6). The synergistic effect between the built-in electric field and the temperature gradient enables carriers to be collected more rapidly within their lifetime, thus enhancing the responsivity and response speed of STGP.

Furthermore, we conduct current-voltage (*I–V*) characterization on these devices. As shown in Figure 3e, the voltage range for the measurement is set between 0 and 10 V in order to deeply study the carrier transport behavior in the device. In Figure 3f–h, the device shows both linear and nonlinear regions within the operating voltage range hinting the different transport mechanism under different voltage [36–38]. At 0–3 V, the curve is linear where the slope of the Log (I)-Log (V) is 1.04 (Figure 3f). This indicates Ohmic contact with minimal potential barrier's effect of the device, and carriers' transport is primarily governed by drift current component [36]. At 3–8 V, the current rises more rapidly than linearly with increasing voltage, approaching an exponential functional form while the slope of the Ln (I) ∼ $V^{1/2}$

is 1.34 (Figure 3g). In this region, the device is dominated by the Schottky emission, where the interfacial barrier is lowered by the applied higher electric filed, facilitating the transition of thermally excited carriers into the conduction band [37]. When the voltage increases from 8 to 10 V, we redraw the plot in Figure 3h based on Ln (I/V^2) as horizontal coordinate and V^{-1} as vertical coordinate. The slope of the curve of Ln (I/V^2) ~ V^{-1} is -13.81. In this region the carriers' transport is based on the Fowler-Nordheim (FN) tunneling which a strong electric field enables carriers to quantum tunnel through the barrier [38].

2.4 | PTE Response of STGP

The in-depth analysis of the built-in electric field, coupled with a detailed investigation of the charge carrier transport mechanism, robustly demonstrates the efficient charge separation and collection capabilities inherent to the Te/Graphene heterostructure. This is critical for PTE detection with high performance. Building upon this optimized charge transportation framework, we subsequently characterized the photodetection performance of the STGP. The STGP we fabricated demonstrated exceptional wide-angle detection, due to its 3D tubular morphology. Light from different angles can illuminate the STGP, inducing localized temperature rise and subsequently generating the temperature gradient through the photothermal effect. This temperature gradient, combined with the built-in electric field at the STGP, drives efficient carrier separation and transport, enabling highly sensitive response to laser with different incident angles. In our work, the wide-angle detection ability is investigated and the experimental configuration is schematically shown in upper-left panel of Figure 4a. When the light incident plane is parallel to the xy plane, effective PTE detection was achieved across a wide angular range from 20 to 160°, where V_{ph} remains higher than $\frac{1}{\sqrt{2}}$ of its maximum value (Figure 4b). When it comes to yz plane, as shown in Figure S12, the relationship between V_{ph} and angle is fitted by a sinusoidal function. In addition, the dependence of V_{ph} and I_{ph} on the incident laser power density shows linear relationships from 0.1 to 100 mW cm^{-2} (Figure 4c; Figure S13), providing strong evidence that the STGP device is capable of effective detection across both high and low intensities of lasers. Here, the responsivities were used to quantitatively evaluate the performance of STGP. The responsivities for voltage (R_v) are defined by [8]:

$$R_v = \frac{V_{ph}}{P_\lambda A_{eff}} \quad (5)$$

where V_{ph} is photovoltage, P_λ is laser power per unit area and A_{eff} is effective illumination area. Here 760 μm^2 was used as A_{eff} based on microscopy image. As a PTE detector, the STGP exhibits a stable and high voltage responsivity across 450–800 nm (Figure S14), indicating the device's excellent photodetection capability over a broad spectral range. In our work, we measured the response of STGP to laser power at wavelengths of 450, 520, 635, and 940 nm, and systematically investigate the relationship between laser power density and the responsivity. It can be observed that for a variation in power density of at least two orders of magnitude, STGP maintains relatively stable responsivity at each wavelength (Figure 4d), which means good consistency at both weak and strong laser illuminations. According to the results, we obtain the highest R_v of 259, 186, 164, and 128 V W^{-1} for lasers of 940, 635, 520, and 450 nm, respectively. Notably, STGP maintains high responsivity across the visible range compared to literature [8] validates that the built-in field at the Te/Graphene interface possesses effective carrier extraction ability. It is worth noting that as the wavelength increases, the energy of incident photons is more efficiently converted into heat, leading to the establishment of a larger temperature gradient [8]. Consequently, a gradual increase in responsivity with increasing light wavelength is observed in Figure 4e and Figure S15. Additionally, the detectivity (D*) achieves 4.39 × 10^{10} Jones under 940 nm laser, as demonstrated in Figure S16. It is worth noting that compared with previous literature [8], the introduction of Graphene lead to slightly lower D* possibly due to higher dark current, although faster carrier extraction is realized in STGP. In addition, we conduct *I–V* characterization on STGP under dark and illuminated situations (Figure S17), which manifest the self-driven ability of the STGP. Figure 4e further provides the photocurrent mapping of a STGP working in self-driven mode, where we could clearly witness that photocurrent progressively decreases for illumination spot moving from Te layer to Te/Graphene heterostructure and then to Graphene. The highest photocurrent corresponds to the highest temperature gradient (ΔT) when Te layer is under laser illumination, which produces the highest photovoltage via the Seebeck effect.

In order to check the polarized light detection performance of STGP, a polarizer and a half-wave plate are incorporated in the laser path (lower-right panel of Figure 4a). The polarization angle is defined as 0° when the electric field vector of the incident light is parallel to the carrier transport direction. Simulations in Figure S18 confirm that compared to the planar device, tubular structure demonstrated stronger interaction with the light with polarizations. More, Figure 4f illustrates the dependence of I_{ph} on the polarization angle of incident lights with wavelengths of 520 nm, and the calculated dichroic ratio is 1.40. This suggests that the efficiency of light-matter coupling differs at different polarization angles (Figure S19), leading to variations in PTE effect. The close values of the polarization ratios for more wavelengths further confirm that the polarization relies on the geometric anisotropy of the STGP, as shown in Figure S20. Therefore, in addition to wide-angle photodetection ability, this device can also be used for polarization-sensitive detection, showcasing great application potential. Furthermore, the stability of the STGP is also important for future practical applications. STGP remains detection stability (6% drop) after a 120-day storage in room temperature and pressure (Figure 4g). The above results confirm that STGP provides outstanding structure and performance stability. Figure 4h and Table S2 systematically illustrate the comparison of the two key parameters: responsivity and response time between our STGP with several existing PTE detectors. A clear trade-off trend can be observed among conventional devices: those with high responsivity often exhibit long response times (on the order of seconds), while devices with fast response speeds generally suffer from low responsivity, limiting their applicability in high-speed imaging and real-time detection [39, 40]. On the other hand, Graphene-based detectors, though demonstrate microsecond-scale response time, often show insufficient responsivity, which restricts their use under low-light conditions [34]. In contrast, our STGP demonstrates a simultaneous breakthrough in both

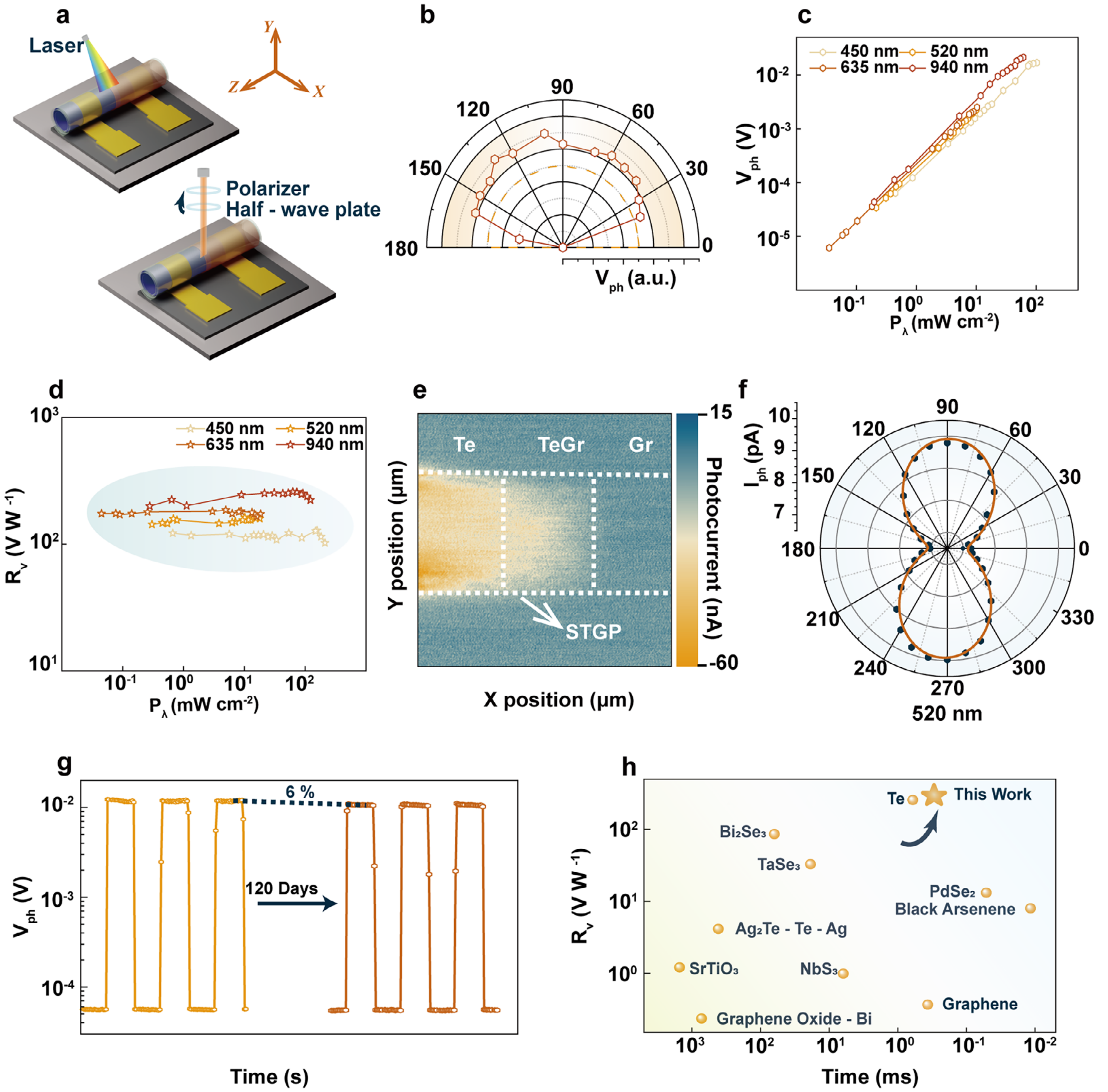

FIGURE 4 | PTE detection performance of STGP. (a) The schematic diagram of the experimental setups for wide-angle photodetection and polarized light detection. (b) V_{ph} under 450 nm laser with different incident angles. (c) V_{ph} as the functions of P_λ for STGP illuminated by 450, 520, 635, and 940 nm lasers. (d) R_v as the functions of P_λ for STGP illuminated by 450, 520, 635, and 940 nm lasers. (e) Photocurrent mapping results of STGP. (f) V_{ph} under 520 nm lasers with different polarized angle. 0° indicates that the electric field vector of the incident light is parallel to the axis of the tubular structure. g) Stability test of STGP after 120 days' exposure in the air and ambient temperature. (h) Comparison of R_v and response time of STGP and other reported PTE detectors.

responsivity and response speed. This outstanding performance stems primarily from the unique tubular heterostructure of the device. The results highlight the potential of STGP while also underscore the significance of heterostructure design and rolled-up engineering in the field of photodetection.

The simultaneous achievement of high responsivity and rapid response speed effectively positioning the STGP as a transformative candidate for advanced optoelectronic imaging. Motivated by these superior device characteristics, we integrated the STGP into a scanning optical system to practically demonstrate its capabilities in image convolution processing. The imaging system is schematically shown in Figure 5a, where patterned incident light is produced by a mask while STGP working in self-driven mode under zero bias acts as the receiver for imaging. The dark blue dashed box indicates the additional optical components required for polarized light imaging: a polarizer and a half-wave plate. The polarizer converts the laser into polarized

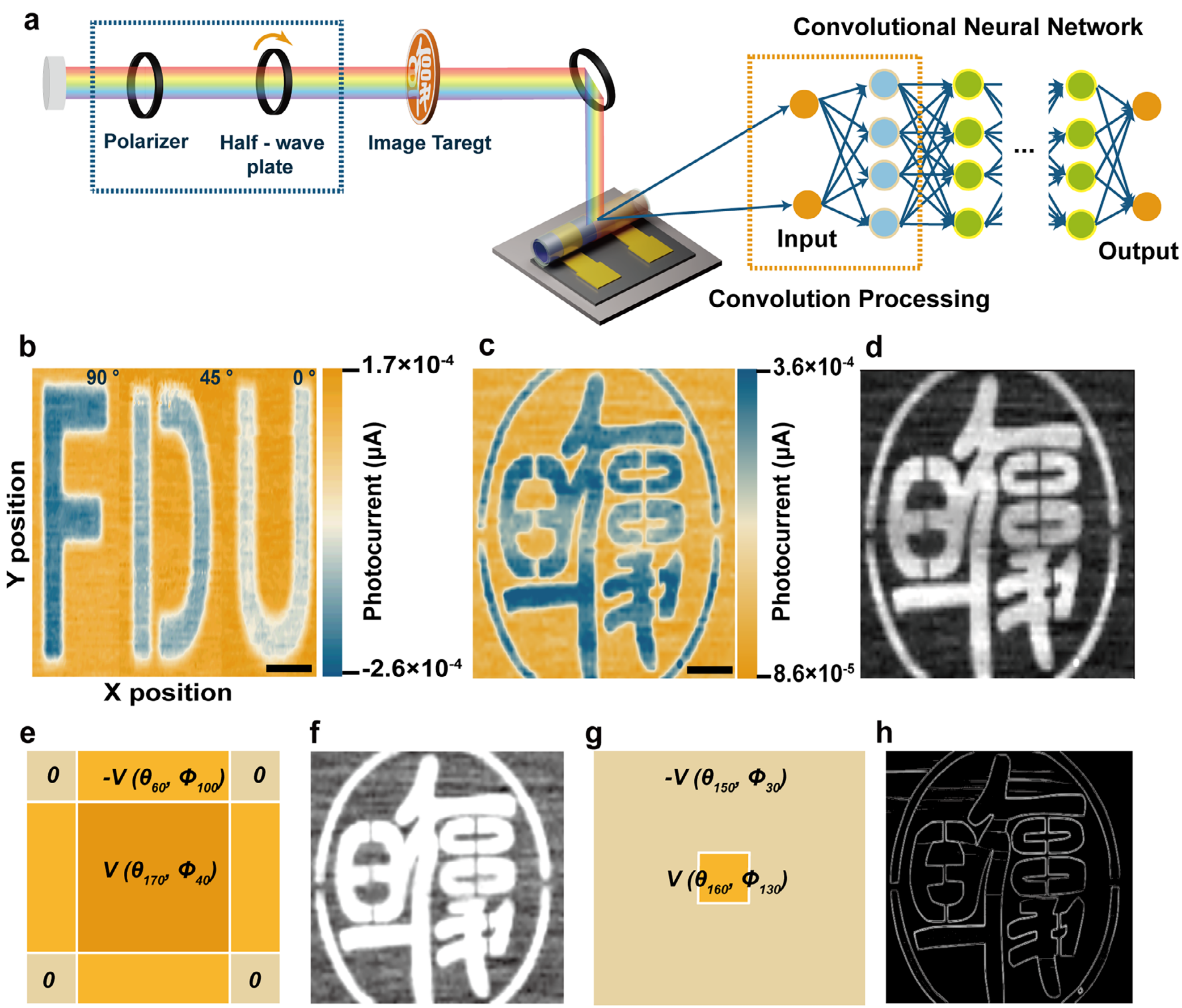

FIGURE 5 | Single-pixel PTE imaging based on STGP. (a) The schematic diagram of the setup for imaging (left panel). The orange dashed line box in the right panel indicates the role of convolution image processing in Convolutional Neural Networks. (b) Imaging of the letters "F", "D", and "U" respectively with the polarized angles of 90°, 45°, and 0°. Scale bar, 10 mm. (c) Imaging of a "Fudan" logo. Scale bar, 50 mm. (d) Converted grayscale image of the "Fudan" logo. (e) Self-construct convolutional kernels used for sharpness. (f) Convolved image after the convolutional processing. g) Self-construct convolutional kernels used for edge extraction. (h) Convolved image after the convolution processing.

light, while rotating the half-wave plate enables imaging with different polarization angles. For image processing (right panel of Figure 5a), we performed convolution on the STGP-derived images by using the wide-angle photovoltage values as the weights of the convolution kernel, and this process plays a crucial role in Convolutional Neural Networks [21]. Figure 5b shows the polarization-sensitive photocurrent imaging results of STGP under 635 nm laser illumination. By adjusting the polarization angle of the incident light (90°, 45°, and 0°), single-pixel imaging of the letter "F", "D", and "U" are successfully obtained. The relatively fast response time and high stability of the STGP provides a crucial foundation for this process. The results also indicate that the geometric advantages of the tubular structure enable highly sensitive photodetection without requiring an external bias. Figure S21 also demonstrates the imaging of "F", "D", and "U" separately by using three lasers without additional polarization components, further indicating the broadband (from visible to infrared) imaging capability of STGP. In addition, Figure 5c clearly shows an imaging result of the "Fudan" logo. To facilitate subsequent convolutional image processing, the acquired image is converted to grayscale, as shown in Figure 5d. Comparing with the traditional imaging convolution processing methods rely on externally pre-defined operators, we utilize the device's response characteristics to light from different incident angles in 3D space (Figure 1f). The photocurrent values obtained under azimuth angles are mapped as elements of the convolution kernels and the details of the convolution kernels can be seen in Figure 5e,g, and Figure S22. It is worth noting that the self-established convolution kernels are derived entirely from experimental data. In practical operation, we use the raw image (Figure 5d) as the input and employed the self-construct convolution kernels to perform both sharpening and edge extraction processing. Specifically, we applied both self-constructed 3 × 3 (Figure S23) and 5 × 5 convolution kernels to the image for sharpening processing (Figure 5f,h). Based on a comparative evaluation of the final image outputs, the 5 × 5 kernel was selected as the optimal choice for the final result. The imaging results processed by other self-constructed convolution kernels are shown in Figures S24a and S25a. Here, we selected the photocurrent values obtained at angles (170°, 40°) and (60°, 100°) to form the convolution kernel for sharpening process, and those at (160°, 130°) and (150°, 30°) to construct the kernel for edge extraction. The sharpening process significantly improves the clarity of image boundaries (Figure 5f), making details in original grayscale image more pronounced while the edge extraction process effectively isolates the contour structures of the target regions (Figure 5h), achieving clear and continuous boundary delineation. The present results not only validate the suitability of the device's output current for constructing image operators but also demonstrate feasibility of self-constructed convolution kernels in the imaging processing. In addition, we also compared the images processed by self-constructed convolution kernels with those processed by traditional kernels (Figures S24b and S25b), which demonstrate that the self-constructed kernels achieve superior performance in both image sharpening and edge extraction.

3 | Conclusions

In summary, we have successfully designed and fabricated high-performance STGP, which realizes a high degree of integration between superior performance and advanced functionality via built-in electric field enhancement and a unique tubular geometry. The STGP achieved a combination of performance metrics, delivering a voltage responsivity of 259 V W^{-1} at 940 nm and an ultrafast response time of 192 µs. This performance surpasses the inherent limitations of conventional PTE devices, thereby validating the efficacy of our design strategy. Furthermore, the device demonstrated a broad spectral response and outstanding environmental stability. From a functional perspective, the self-rolled-up tubular geometry provided an unparalleled geometric advantage, enabling both wide-angle detection and intrinsic polarization sensitivity. Critically, we utilized the STGP's measured angle-dependent photocurrent response in 3D space and directly mapped these physical values into the elements of a self-construct convolution kernels. This physics-response-driven computational method was successfully applied to achieve image sharpening and edge extraction, showcasing the high quality of the self-construct kernels. By tightly integrating the device's inherent optical response from wide-angle photocurrent with computational functions from convolution process, this methodology provides strong theoretical and experimental support for the future development of advanced optical sensing and integrated in-sensor visual computing systems.

4 | Experimental Section

4.1 | Fabrication of STGPs

10 nm Ge layer was deposited on the thermal silicon oxide wafer (500 nm SiO_2 layer on Si wafer) by E-beam evaporation (Lab 18, Kurt Lesker) as the sacrificial layer. SiN_x was then deposited by Inductively Coupled Plasma Chemical Vapor Deposition (ICP-CVD, PlasmaPro 100) at 13.56 MHz as the pre-strained layer. Specifically, 15 nm compressive SiN_x was deposited at the pressure of 10 mTorr (RF power 30 W, ICP power 20 W, SiH_4: N_2 = 13.5: 10) and 15 nm tensile SiN_x was deposited at the same pressure of 12 mTorr (RF power 10 W, ICP power 20 W, SiH_4: N_2 = 13.5: 10). Applying 99.9% Te target (from ZhongNuo Advanced Material Technology Co., Ltd), Te layer was deposited by magnetron sputtering (PVD 75, Kurt Lesker) at room temperature (50 sccm Ar, RF power 35 W), and medium Te thickness of 38 nm was chosen for following device fabrication. In the experiment, we performed rapid thermal annealing on Te at 260°C for 10 min to promote its performance. The Graphene on copper foil was a commercial product from PrMat. Thick Poly (methyl methacrylate) (PMMA) layer was spin-coated on Graphene respectively at 1500 and 3000 rpm for 30 s, which provides sufficient mechanical support during the transfer process, and then heated on a hot plate at 160°C for 15 min. Then, the PMMA/Graphene/copper foil was immersed into copper etchant $(NH_4)_2S_2O_8$: H_2O = 10:1) for 1 h to release PMMA/Graphene from the copper foil. The released PMMA/Graphene was cleaned by acetone, ethanol, and deionized water (three times each) and transferred onto Te layer. The sample was immersed in acetone at 40°C for 120 min to remove PMMA completely. Furthermore, the lithography was applied to pattern the nanomembrane. 10 nm Ti and 25 nm Au layers were deposited by E-beam evaporation (DE400, DE Technology Limited) and patterned by photolithography as electrodes. 10 nm Al_2O_3 was deposited by ALD at 130°C for protection during the etching process. XeF_2 vapor was applied to selectively etch the sacrificial Ge layer by XeF_2. The above process is schematically shown in Figure S1.

4.2 | Microstructural Characterizations

XRD analysis was performed by Bruker D8 Advance. Raman characterizations were carried out on Renishaw inVia Qontor Raman spectrometer. The infrared absorption spectrum was tested by FTIR at ATR mode (Bruker VERTEX 70). The observation of STGP was achieved by SEM (Zeiss Sigma 300). KPFM were tested on Oxford cypher s. UPS spectra were tested on ESCALAB Xi. XPS curves were tested on Thermo ESCALAB 250XI.

4.3 | Thermal and Optical Simulation

All simulation about electrical field and temperature distribution was obtain by finite element analysis. STGP structure was simplified as a tubular structure (inner radii was set to be 19 µm) and the wall was Graphene/Te/compressive-SiN_x/tensile-SiN_x nanomembrane (thickness of each layer was set to be separately 1 nm/36 nm/20 nm/20 nm). The boundary condition was programmed as the perfect matching layer. The physical parameters necessary for the numerical modeling of the device were defined for both optical and thermal simulations. For the optical simulation, the material refractive indices were designated as 4.92 for Te layer and 1.98 for SiN_x respectively [41, 42]. The wavelength-dependent refractive index and extinction coefficient of Te layer were obtained from the literature [43].

4.4 | Characterizations of Device Performance

The optoelectrical properties of the STGP were characterized at room temperature using a Keysight B2902B. For photovoltage signal extraction, the measurement setup was employed consisting of a Keysight 33500B waveform generator, a Stanford Research Systems SR830 DSP lock-in amplifier, and a Stanford Research Systems SR570 low-noise current preamplifier. Lasers with the wavelengths of 450, 520, 635, and 940 nm were used as the light sources. The corresponding response time was tested under 940 nm laser with the power density of 122 mW cm^{-2}. Meanwhile, polarized photodetection measurements were conducted by semiconductor parameter analyzer (METATEST Corporation, Metatest E2). Lasers with the wavelengths of 635, 830, 940, and 1550 nm were used as the light sources. The wide-angle photodetection characterization of STGP was performed using a home-made hemispherical setup in Figure S8. The light source was 450 nm laser with power of 169 μw and spot size of ∼20 cm^2. The photocurrent mapping was conducted using scanning photocurrent microscopy based on Raman system WITec, Alpha 300R, and 635 nm laser was used as light source.

4.5 | Calculation of Charge-Density Difference and Electronic Structure

First-principles calculations were performed using the Vienna Ab initio Simulation Package (VASP) based on density functional theory (DFT) with the projector augmented wave (PAW) method and the PBE functional [44–46]. A plane-wave cutoff energy of 500 eV was employed, and DFT-D3 corrections were included to describe the interlayer van der Waals interactions. A 12 × 12 × 1 Gamma-centered k-point grid was used for the DOS and charge density difference calculations, while the electronic band structure was computed along the M-K-Γ-M high-symmetry path with a strict energy convergence of 10^{-7} eV. To reveal the interfacial charge transfer, the charge density difference was obtained by subtracting the charge densities of the isolated Te and Graphene monolayers from that of the total heterostructure. A vacuum layer of 10 Å was set to reduce the effect of adjacent Te/Graphene slabs. The charge-density difference ($\Delta\rho$) was calculated by:

$$\Delta\rho = \Delta\rho_{\mathrm{Te/Graphene}} - \Delta\rho_{\mathrm{Graphene}} - \Delta\rho_{\mathrm{Te}} \tag{6}$$

Here, $\Delta\rho_{\mathrm{Te/Graphene}}$, $\Delta\rho_{\mathrm{Graphene}}$ and $\Delta\rho_{\mathrm{Te}}$represent the total charge densities of the Te/Graphene heterostructure, the Graphene, and the Te layer, respectively.

Acknowledgements

This work is supported by the National Key Technologies R&D Program of China (2021YFA0715302), the National Natural Science Foundation of China (92580128, 525B1002, 62375054, 523B2107, 62525407, and 62334010), the Science and Technology Commission of Shanghai Municipality (25CL2900202, 24520750200, and 24CL2900202), the Natural Science Foundation of Jilin Province (20250101001JJ), and Changchun Key Research and Development Program (23GZZ11). Parts of the sample fabrication were performed at Fudan Nano-fabrication Lab, Micro-and Nanofabrication Lab at Yiwu Research Institute of Fudan University, ShanghaiTech Quantum Device Lab, and ShanghaiTech Soft Matter Nanofab (No. SMN180827).

Funding

National Key Technologies R&D Program of China (2021YFA0715302), the National Natural Science Foundation of China (92580128, 525B1002, 62375054, 523B2107, 62525407, and 62334010), the Science and Technology Commission of Shanghai Municipality (25CL2900202, 24520750200, and 24CL2900202), the Natural Science Foundation of Jilin Province (20250101001JJ), and Changchun Key Research and Development Program (23GZZ11).

Conflicts of Interest

The authors declare no conflicts of interest.

Data Availability Statement

The data that support the findings of this study are available from the corresponding author upon reasonable request.

References

1. Z. Sun and H. Chang, "Graphene and Graphene-Like Two-dimensional Materials in Photodetection: Mechanisms and Methodology," *ACS Nano* 8 (2014): 4133–4156.

2. T. Mueller, F. Xia, and P. Avouris, "Graphene Photodetectors for High-speed Optical Communications," *Nature Photonics* 4 (2010): 297–301.

3. Y. Lu, C. Lin, and C. Shan, "Optoelectronic Diamond: Growth, Properties, and Photodetection Applications," *Advanced Optical Materials* 6 (2018): 1800359.

4. W. Lee, Y. Liu, Y. Lee, et al., "Two-Dimensional Materials in Functional Three-Dimensional Architectures with Applications in Photodetection and Imaging," *Nature Communications* 9 (2018): 1417.

5. X. Lu, L. Sun, P. Jiang, and X. Bao, "Progress of Photodetectors Based on the Phototh Ermoelectric Effect," *Advanced Materials* 31 (2019): 1902044.

6. M. Dai, X. Zhang, and Q. Wang, "2D Materials for Photothermoelectric Detectors: Mechanisms, materials, and Devices," *Advanced Functional Materials* 34 (2024): 2312872.

7. L. Liu, J. Gou, H. Dou, et al., "Fast-Response, Broadband Si-based Photothermoelectric Photodetector Based on RF-Sputtering PbTe Film," *ACS Photonics* 11 (2024): 4751–4760.

8. J. Huang, C. You, B. Wu, et al., "Enhanced Photothermoelectric Conversion in Self-Rolled Tellurium Photodetector with Geometry-Induced Energy Localization," *Light: Science & Applications* 13 (2024): 153.

9. Z. Zhang, T. Cai, Z. Li, et al., "Graphene Readout Silicon-based Microtube Photodetectors for Encrypted Visible Light Communication," *Advanced Materials* 37, (2025): 2413771.

10. B. Wu, Z. Zhang, B. Chen, et al., "One-step Rolling Fabrication of VO_2 Tubular Bolometers with Polarization-Sensitive and Omnidirectional Detection," *Science Advances* 9 (2023): adi7805.

11. S. Liu, Y. Ding, W. Rong, et al., "Working Voltage Switching the Photo-/Thermo-Electric Effect for Distinct Ultraviolet and Infrared Signal Detection," *ACS Nano* 18 (2024): 25226–25236.

12. J. Zhang, R. Sun, Z. Hu, J. Tian, and Z. Liu, "Photo-thermoelectric Response in Graphene/h-BN Heterostructures Induced by Interface Thermal Asymmetry for Enhanced Photodetection," *ACS Applied Nano Materials* 8 (2025): 21337–21345.

13. H. Cho, I. Lee, J. Jang, et al., "Real-Time Finger Motion Recognition Using Skin-conformable Electronics," *Nature Electronics* 6 (2023): 619–629.

14. L. Pi, P. Wang, S.-J. Liang, et al., "Broadband Convolutional Processing Using Band-Alignment-Tunable Heterostructures," *Nature Electronics* 5 (2022): 248–254.

15. S. Lee, R. Peng, C. Wu, and M. Li, "Programmable Black Phosphorus Image Sensor for Broadband Optoelectronic Edge Computing," *Nature Communications* 13 (2022): 1485.

16. D. Francis and K. Raimond, “Major Advancements in Kernel Function Approximation,” *Artificial Intelligence Review* 54 (2021): 843–876.

17. Z. Wang, T. Wan, S. Ma, and Y. Chai, “Multidimensional Vision Sensors for Information Processing,” *Nature Nanotechnology* 19 (2024): 919–930.

18. J. Feldmann, N. Youngblood, M. Karpov, et al., “Parallel Convolutional Processing Using an Integrated Photonic Tensor Core,” *Nature* 589 (2021): 52–58.

19. Y. Yu, T. Xiong, Z. Zhou, et al., “Spectrum-Dependent Image Convolutional Processing via a Two-Dimensional Polarization-Sensitive Photodetector,” *Nano Letters* 24 (2024): 6788–6796.

20. T. Li, J. Miao, X. Fu, et al., “Reconfigurable, Non-volatile Neuromorphic Photovoltaics,” *Nature Nanotechnology* 18 (2023): 1303–1310.

21. H. Jang, H. Hinton, W.-B. Jung, et al., “In-sensor Optoelectronic Computing Using Electrostatically Doped Silicon,” *Nature Electronics* 5 (2022): 519–525.

22. K. Roy, J. Akhilesh, and P. Priyadarshini, “Towards Spike-based Machine Intelligence with Neuromorphic Computing,” *Nature* 575 (2019): 607–617.

23. C. Xu, R. Pan, Q. Guo, et al., “Ultrathin Silicon Nanomembrane in a Tubular Geometry for Enhanced Photodetection,” *Advanced Optical Materials* 7 (2019): 1900823.

24. H. Wang, H. Zhen, S. Li, et al., “Self-rolling and Light-trapping in Flexible Quantum Well–embedded Nanomembranes for Wide-angle Infrared Photodetectors,” *Science Advances* 2 (2016): 1600027.

25. L. Wang, Z. Tian, B. Zhang, et al., “On-Chip Rolling Design for Controllable Strain Engineering and Enhanced Photon–Phonon Interaction in Graphene,” *Small* 15 (2019): 1805477.

26. B. Wu, Z. Zhang, Z. Zheng, et al., “Self-Rolled-up Ultrathin Single-Crystalline Silicon Nanomembranes for on-Chip Tubular Polarization Photodetectors,” *Advanced Materials* 35 (2023): 2306715.

27. W. Huang, S. Koric, X. Yu, K. Hsia, and X. Li, “Precision Structural Engineering of Self-Rolled-up 3D Nanomembranes Guided by Transient Quasi-static FEM Modeling,” *Nano Letters* 14 (2014): 6293–6297.

28. G. Nikishkov, “Curvature Estimation for Multilayer Hinged Structures with Initial Strains,” *Journal of Applied Physics* 94 (2003): 5333–5336.

29. Z. Zhang, B. Wu, Y. Wang, et al., “Multilevel Design and Construction in Nanomembrane Rolling for Three-Dimensional Angle-Sensitive Photodetection,” *Nature Communications* 15 (2024): 3066.

30. R. Ziolo and J. Troup, “Experimental Observation of the Tellurium (IV) Bonding and Lone-pair Density in Dimethyltellurium Dichloride by X-ray Diffraction Techniques,” *Journal of the American Chemical Society* 105 (1983): 229–235.

31. J.-K. Qin, P.-Y. Liao, M. Si, et al., “Raman Response and Transport Properties of Tellurium Atomic Chains Encapsulated in Nanotubes,” *Nature Electronics* 3 (2020): 141–147.

32. W. Jie, Y. Hui, Y. Zhang, S. Lau, and J. Hao, “Effects of Controllable Biaxial Strain on the Raman Spectra of Monolayer Graphene Prepared by Chemical Vapor Deposition,” *Applied Physics Letters* 102 (2013): 223112.

33. K. Momma and F. Izumi, “VESTA 3 for Three-dimensional Visualization of Crystal, Volumetric and Morphology Data,” *Journal of Applied Crystallography* 44 (2011): 1272–1276.

34. F. Bonaccorso, Z. Sun, T. Hasan, and A. Ferrari, “Graphene Photonics and Optoelectronics,” *Nature Photonics* 4 (2010): 611–622.

35. P. Meng, Y. Yu, Z. Wang, et al., “Room-Temperature Blackbody-Sensitive and Fast Infrared Photodetectors Based on 2D Tellurium/Graphene van der Waals Heterojunction,” *ACS Photonics* 9 (2022): 1775–1782.

36. V. Mihailetchi, J. Wildeman, and P. Blom, “Space-charge Limited Photocurrent,” *Physical Review Letters* 94 (2005): 126602.

37. J.-G. Park, W.-S. Nam, S.-H. Seo, et al., “Multilevel Nonvolatile Small-Molecule Memory Cell Embedded with Ni Nanocrystals Surrounded by a NiO Tunneling Barrier,” *Nano Letters* 9 (2009): 1713–1719.

38. H. Sun, Q. Liu, S. Long, H. Lv, W. Banerjee, and M. Liu, “Multilevel Unipolar Resistive Switching with Negative Differential Resistance Effect in Ag/SiO_2/Pt Device,” *Journal of Applied Physics* 116 (2014): 154509.

39. Y. Zhang, Y. Meng, L. Wang, et al., “Pulse Irradiation Synthesis of Metal Chalcogenides on Flexible Substrates for Enhanced Photothermoelectric Performance,” *Nature Communications* 15 (2024): 728.

40. B. Zhu, J.-J. Wu, D. Li, et al., “Orientation-related Giant Photothermoelectric Energy Conversion in Quasi-One-Dimensional Van Der Waals $TaSe_3$ Crystals,” *ACS Nano* 18 (2024): 35696–35704.

41. R. S. Caldwell and H. Fan, “Optical Properties of Tellurium and Selenium,” *Physical Review* 114 (1959): 664–675.

42. J. Lukeš, V. Hájková, M. Hlubučková, V. Kanclíř, and K. Žídek, “Sensitive Detection of Si_3N_4 Thin-film Defects via Second Harmonic Generation Microscopy,” *Optics Letters* 50 (2025): 1885–1888.

43. Y. Xia, L. Peng, L. Shu, et al., “Strong Intervalley Scattering-induced Renormalization of Electronic and Thermal Transport Properties and Selection Rule Analysis in 2D Tellurium,” *ACS Nano* 18 (2024): 5814–5827.

44. G. Kresse and J. Furthmüller, “Efficient Iterative Schemes for Ab Initio Total-Energy Calculations Using a Plane-wave Basis Set,” *Physical Review B* 54 (1996): 11169–11186.

45. G. Kresse and D. Joubert, “From Ultrasoft Pseudopotentials to the Projector Augmented-wave Method,” *Physical Review B* 59 (1999): 1758–1775.

46. J. Perdew, K. Burke, and M. Ernzerhof, “Generalized Gradient Approximation Made Simple,” *Physical Review Letters* 77 (1997): 3868.

Supporting Information

Additional supporting information can be found online in the Supporting Information section.

Supporting File: adom71223-sup-0001-SuppMat.docx.